

2012

Thermal-Based Evaporative Stress Index for Monitoring Surface Moisture Depletion

Martha C. Anderson

USDA-ARS, martha.anderson@ars.usda.gov

Christopher R. Hain

National Oceanic and Atmospheric Administration, christopher.hain@nasa.gov

Brian D. Wardlow

University of Nebraska - Lincoln, bwardlow2@unl.edu

Agustin Pimstein


The Pontifical Catholic University of Chile

John R. Mecikalski

University of Alabama in Huntsville

See next page for additional authors

Follow this and additional works at: <https://digitalcommons.unl.edu/droughtfacpub>

 Part of the [Climate Commons](#), [Environmental Indicators and Impact Assessment Commons](#), [Environmental Monitoring Commons](#), [Hydrology Commons](#), [Other Earth Sciences Commons](#), and the [Water Resource Management Commons](#)

Anderson, Martha C.; Hain, Christopher R.; Wardlow, Brian D.; Pimstein, Agustin; Mecikalski, John R.; and Kustas, William P., "Thermal-Based Evaporative Stress Index for Monitoring Surface Moisture Depletion" (2012). *Drought Mitigation Center Faculty Publications*. 106.

<https://digitalcommons.unl.edu/droughtfacpub/106>

This Article is brought to you for free and open access by the Drought -- National Drought Mitigation Center at DigitalCommons@University of Nebraska - Lincoln. It has been accepted for inclusion in Drought Mitigation Center Faculty Publications by an authorized administrator of DigitalCommons@University of Nebraska - Lincoln.

Authors

Martha C. Anderson, Christopher R. Hain, Brian D. Wardlow, Agustin Pimstein, John R. Mecikalski, and William P. Kustas

Published in *Remote Sensing of Drought: Innovative Monitoring Approaches*, edited by Brian D. Wardlow, Martha C. Anderson, & James P. Verdin (CRC Press/Taylor & Francis, 2012).

This chapter is a U.S. government work and is not subject to copyright in the United States.

Authors:

Martha C. Anderson

Hydrology and Remote Sensing Laboratory
Agricultural Research Service
U.S. Department of Agriculture
Beltsville, Maryland

Christopher R. Hain

National Environmental Satellite, Data, and Information Service
National Oceanic and Atmospheric Administration
Camp Springs, Maryland

Brian D. Wardlow

National Drought Mitigation Center
School of Natural Resources
University of Nebraska–Lincoln
Lincoln, Nebraska

Agustin Pimstein

Faculty of Agronomy and Forestry Engineering
Department of Fruit Production and Enology
The Pontifical Catholic University of Chile
Santiago, Chile

John R. Mecikalski

Department of Atmospheric Science
University of Alabama in Huntsville
Huntsville, Alabama

William P. Kustas

Hydrology and Remote Sensing Laboratory
Agricultural Research Service
U.S. Department of Agriculture
Beltsville, Maryland

7 Thermal-Based Evaporative Stress Index for Monitoring Surface Moisture Depletion

*Martha C. Anderson, Christopher R. Hain,
Brian D. Wardlow, Agustin Pimstein,
John R. Mecikalski, and William P. Kustas*

CONTENTS

7.1	Introduction	145
7.2	TIR-Based Modeling of Evapotranspiration	147
7.3	Evaporative Stress Index.....	150
7.4	Precipitation-Based Drought Metrics	152
7.4.1	Palmer Indices	152
7.4.2	Standardized Precipitation Index	152
7.4.3	U.S. Drought Monitor	153
7.4.4	Standardized Anomalies and Seasonal Composites.....	154
7.5	Drought Index Intercomparison	154
7.5.1	Seasonal Anomalies.....	154
7.5.2	Monthly Comparisons	156
7.5.3	Spatiotemporal Correlations between Indices	157
7.6	Limitations and Future Work	160
7.7	Conclusions	162
	Acknowledgments.....	164
	References.....	164

7.1 INTRODUCTION

The standard suite of indicators currently used in operational drought monitoring reflects anomalous conditions in several major components of the hydrologic budget—representing deficits in precipitation, soil moisture content, runoff, surface and groundwater storage, snowpack, and streamflow. In principle, it is useful to have a diversity of indices because drought can assume many forms (meteorological, agricultural, hydrological, and socioeconomic), over broad ranges in timescale

(weeks to years), and with varied impacts of interest to different stakeholder groups. Farmers, for example, may be principally interested in soil moisture deficits, river forecasters will focus on streamflow fluctuations, and water managers will be concerned with longer-term stability in municipal water supply and reservoir levels. Only recently has actual evapotranspiration (ET) been considered as a primary indicator of drought conditions (e.g., Anderson et al., 2007b; Labedzki and Kanecka-Geszke, 2009; Li et al., 2005; Mo et al., 2010). ET is a valuable drought indicator because it reflects not only moisture availability but also the rate at which water is being consumed. Because transpiration (T) and carbon uptake by vegetation are tightly coupled through stomatal exchange, ET anomalies are indicative of vegetation health and growing conditions. In addition, the importance of so-called flash droughts is becoming increasingly evident, where hot, dry, and windy atmospheric conditions can lead to unusually rapid soil moisture depletion and, in some cases, devastating crop failure. Such events cannot be easily identified using local precipitation anomalies but should have a detectable ET signature.

In general, techniques for mapping ET can be classified into either prognostic or diagnostic modeling approaches. Prognostic approaches, like the land-surface models (LSMs) implemented within the National Land Data Assimilation System (NLDAS; Mitchell et al., 2004), use spatially distributed observations of precipitation as input to compute the full water balance at every model grid cell, considering soil texture and moisture holding capacity, runoff, and the local rate of infiltration and drainage. Such models are extremely useful in drought monitoring because they can generate self-consistent anomaly indicators relating to each component of the surface water budget. However, accurate assessment of critical model inputs can be challenging, particularly for large-scale applications. Real-time precipitation analyses of reasonable quality are available over most of the United States (e.g., McEnery et al., 2005), but many parts of world lack sufficiently dense radar and rain-gauge networks to generate comparable data sets. Satellite-derived global precipitation products provide improved spatial coverage over these data-limited areas (Huffman et al., 2007; Joyce et al., 2004) but are known to exhibit seasonally and spatially dependent biases (Villarini et al., 2009; Zeweldi and Gebremichael, 2009) and often rely on gauge correction to produce realistic rainfall amounts. Soil moisture storage, runoff, and infiltration are strongly determined by the assumed soil properties, which are typically linked to soil type and may have high uncertainties. Biased specifications of precipitation rates and soil hydraulic properties can introduce significant cumulative biases into prognostic water budget estimates (Schaake et al., 2004), with potentially deleterious effects on climatologies derived for drought monitoring. Furthermore, LSM predictions will not reflect non-precipitation-related moisture inputs to the local land-surface system (e.g., irrigation or influence of shallow groundwater) unless these inputs are explicitly modeled.

In contrast, diagnostic ET mapping techniques typically require significantly less a priori knowledge of antecedent moisture inputs and subsurface conditions. These methods use remote-sensing measurements of key land-surface state variables to “diagnose” the current surface moisture status. Because evaporation cools surfaces, the land-surface temperature (LST) state conveys valuable proxy information regarding soil moisture and is commonly used in diagnostic estimates of

ET (Courault et al., 2005; Kalma et al., 2008; Norman et al., 1995b). The observed LST implicitly reflects all moisture inputs to the land-surface system, both known (precipitation) and unknown (e.g., natural or anthropogenic groundwater extraction), and, therefore, these inputs do not need to be explicitly specified as in the prognostic modeling approach. Diagnostic ET models therefore provide information about actual water consumption, which may exceed local short-term moisture inputs when water is mined or manually transferred between basins. This information is a valuable supplement to the “natural consumption” estimates typically conveyed by prognostic water balance models.

In this chapter, we discuss a new drought index based on diagnostic remote sensing of ET. The Evaporative Stress Index (ESI) represents temporal anomalies in the ratio of actual ET to potential ET (PET), derived from satellite imagery collected in the thermal infrared (TIR) atmospheric window channel (10–12 μm). TIR imagery is used to compute LST, which serves as a boundary condition on the surface energy balance, including the evaporative flux. The modeling system used here is multiscale, running over continental scales using TIR imagery acquired with the Geostationary Operational Environmental Satellites (GOES) combined with short-wave information about vegetation cover fraction to diagnose evaporative fluxes at 5–10 km spatial resolution using the Atmosphere-Land Exchange Inverse Model (ALEXI; Anderson et al., 2007b). Higher resolution assessments of surface moisture stress can be obtained through spatial disaggregation (DisALEXI; Norman et al., 2003) using TIR data from polar orbiting systems such as Landsat, the Advanced Spaceborne Thermal Emission and Reflection Radiometer (ASTER), and the Moderate Resolution Imaging Spectroradiometer (MODIS), which image at resolutions ranging between 100 and 1000 m. Because the ESI does not use rainfall data as input, it provides an independent check on precipitation-based drought indicators and may be more robust in regions with minimal ground-based meteorological infrastructure. The remotely sensed ET fields have the advantage that they inherently include non-precipitation-related moisture signals that need to be modeled a priori in prognostic LSM schemes.

Here we compare the ESI with standard precipitation-based drought indices and with drought classifications recorded over the continental United States (CONUS) in retrospective U.S. Drought Monitor (USDM; Svoboda et al., 2002) maps from 2000 to 2009. The goal of this analysis is to establish the level of similarity between ET- and precipitation-based indices and to identify new and unique information regarding drought conditions that only diagnostic ET estimates can provide.

7.2 TIR-BASED MODELING OF EVAPOTRANSPIRATION

The ALEXI surface energy balance model (Anderson et al., 1997, 2007b,c; Mecikalski et al., 1999) was specifically designed to minimize the need for ancillary meteorological data while maintaining a physically realistic representation of land-atmosphere exchange over a wide range of vegetation cover conditions. It is one of few diagnostic LSMs designed explicitly to exploit the high temporal resolution afforded by geostationary satellites like GOES, which is ideal for operational large-area applications such as drought monitoring.

Surface energy balance models estimate ET by partitioning the energy available at the land surface ($RN - G$, where RN is net radiation and G is the soil heat conduction flux, in W m^{-2}) into turbulent fluxes of sensible and latent heating (H and λE , respectively, in W m^{-2}):

$$RN - G = H + \lambda E \quad (7.1)$$

where,

λ is the latent heat of vaporization (J kg^{-1})

E is ET ($\text{kg s}^{-1} \text{m}^{-2}$ or mm s^{-1})

Surface temperature is a valuable metric for constraining λE because varying soil moisture conditions yield a distinctive thermal signature. Moisture deficiencies in the root zone lead to vegetation stress and elevated canopy temperatures, while depletion of water from the soil surface layer causes the soil component of the scene to heat up rapidly.

The land-surface representation in the ALEXI model is based on the series version of the two-source energy balance (TSEB) model of Norman et al. (1995a) (see also Kustas and Norman, 1999, 2000), which partitions the composite surface radiometric temperature, T_{RAD} , into characteristic soil and canopy temperatures, T_S and T_C , based on the local vegetation cover fraction apparent at the thermal sensor view angle, $f(\theta)$:

$$T_{RAD}(\theta) \approx \left(f(\theta)T_C^4 + [1 - f(\theta)]T_S^4 \right)^{1/4} \quad (7.2)$$

(see schematic in [Figure 7.1](#)). For a canopy with a spherical leaf angle distribution and leaf area index (LAI), $f(\theta)$ can be approximated as

$$f(\theta) = 1 - \exp\left(\frac{-0.5\Omega(\theta)LAI}{\cos\theta}\right) \quad (7.3)$$

where $\Omega(\theta)$ is a view angle–dependent clumping factor, currently assigned by vegetation class (Anderson et al., 2005). With information about T_{RAD} , LAI , and radiative forcing, the TSEB evaluates the soil (subscript “s”) and the canopy (subscript “c”) energy budgets separately, computing system and component fluxes of net radiation ($RN = RN_C + RN_S$), sensible and latent heat ($H = H_C + H_S$ and $\lambda E = \lambda E_C + \lambda E_S$), and soil heat conduction (G). Importantly, because angular effects are incorporated into the decomposition of T_{RAD} , the TSEB can accommodate thermal data acquired at off-nadir viewing angles and can therefore be applied to geostationary satellite images.

The TSEB has a built-in mechanism for detecting thermal signatures of vegetation stress. A modified Priestley–Taylor relationship (PT; Priestley and Taylor, 1972), applied to the divergence of net radiation within the canopy (RN_C), provides an initial estimate of canopy transpiration (λE_C), while the soil evaporation rate (λE_S) is computed as a residual to the system energy budget. If the vegetation is stressed and transpiring at significantly less than the potential rate, the PT equation will overestimate

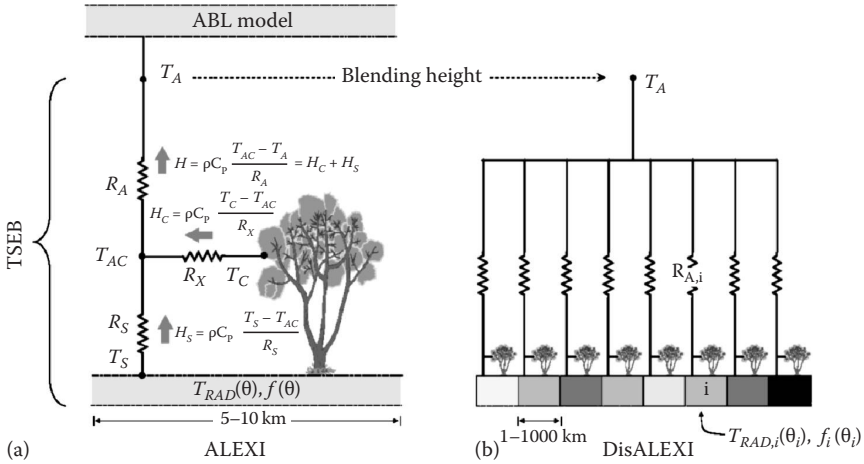


FIGURE 7.1 Schematic diagram representing the ALEXI (a) and DisALEXI (b) modeling schemes, highlighting fluxes of sensible heat (H) from the soil and canopy (subscripts “s” and “c”) along gradients in temperature (T), and regulated by transport resistances R_A (aerodynamic), R_x (bulk leaf boundary layer), and R_s (soil surface boundary layer). DisALEXI uses the air temperature predicted by ALEXI near the blending height (T_A) to disaggregate 10 km ALEXI fluxes, given vegetation cover ($f(\theta)$) and directional surface radiometric temperature ($T_{RAD}(\theta)$) information derived from high-resolution remote-sensing imagery at look angle θ .

λE_C and the residual λE_S will become negative. Condensation onto the soil is unlikely during midday on clear days, and, therefore, $\lambda E_S < 0$ is considered a signature of system stress. Under such circumstances, the PT coefficient is iteratively throttled back until $\lambda E_S \sim 0$ (expected under dry conditions). Both λE_C and λE_S will then be some fraction of the PET rates associated with the canopy and soil. This approach therefore opens the potential for surface and root zone moisture pool assessment and, thus, concomitant tracking of both meteorological and agricultural drought.

For regional-scale applications, the TSEB has been coupled with an atmospheric boundary layer (ABL) model to internally simulate land–atmosphere feedback on near-surface air temperature (T_A in Figure 7.1). In the ALEXI model, the TSEB is applied at two times during the morning ABL growth phase (~1 h after sunrise and before local noon) using radiometric temperature data obtained from a geostationary platform like GOES at spatial resolutions of 5–10 km. Energy closure over this interval is provided by a simple slab model of ABL development (McNaughton and Spriggs, 1986), which relates the rise in air temperature in the mixed layer to the time-integrated influx of sensible heat from the land surface. As a result of this configuration, ALEXI uses only time-differential temperature signals, thereby minimizing flux errors due to absolute sensor calibration, as well as atmospheric and emissivity corrections (Kustas et al., 2001). The primary radiometric signal is the morning surface temperature rise, while the ABL model component uses only the general slope (lapse rate) of the atmospheric temperature profile (Anderson et al., 1997), which is more reliably analyzed from synoptic radiosonde data than is the absolute temperature reference.

Anderson et al. (2007a) summarize ALEXI validation experiments employing a spatial flux disaggregation technique (DisALEXI; Norman et al., 2003), which uses higher resolution TIR imagery presently only available from aircraft or polar orbiting systems like Landsat, ASTER, or MODIS to downscale the GOES-based flux estimates (10 km resolution) to the flux measurement footprint scale (on the order of 100–1000 m; see Figure 7.1). Typical root-mean-square deviations in comparison with tower flux measurements (30 min averages) of H and λE are 35–40 W m⁻² (15% of the mean observed flux) over a range of vegetation cover types and climatic conditions, while errors at daily time steps are typically 10%. Disaggregation also facilitates high spatial resolution assessment of moisture flux and stress conditions, supporting a broader range of local-scale decision-making activities than can be serviced with the coarser-resolution ALEXI results and providing detailed insights into landscape-level ET dynamics. However, high-resolution ET mapping is constrained in temporal resolution by the overpass frequency of the polar orbiting satellite.

A complete ALEXI processing infrastructure has been developed to automatically ingest and preprocess all required input data, to execute the model, and to postprocess model output for visual display and use in other applications. The model currently runs daily on a 10 km resolution grid covering the CONUS, and to date, model input/output from this framework has been archived for the period 2000 to present. Snow-covered regions are currently masked using the 24 km resolution Daily Northern Hemisphere Snow and Ice Analysis product distributed through the National Snow and Ice Data Center (NSIDC; http://nsidc.org/data/docs/noaa/g02156_ims_snow_ice_analysis/index.html).

7.3 EVAPORATIVE STRESS INDEX

In this chapter, we explore applications of remotely sensed ET to drought monitoring. In particular, we examine information conveyed by anomalies in the ratio of actual to PET :

$$f_{PET} = \frac{ET}{PET} \quad (7.4)$$

determined under clear-sky conditions. In this analysis, ET and PET are instantaneous estimates at shortly before local noon, retrieved using ALEXI. Equation 7.4 follows from earlier work using TIR band data in agricultural applications, as reviewed by Moran (2003), where f_{PET} has been used as a tool for crop stress detection and irrigation scheduling. Limiting the assessment to clear-sky conditions separates variability in ET due to soil moisture from impacts of varying cloud climatology. In addition, TIR-based LST retrieval can be accomplished only through clear skies. Division by PET serves to normalize out some degree of variability in ET due to seasonal variations in available energy and vegetation cover amount, further refining the focus on the soil moisture signal. Standardized anomalies in f_{PET} will be referred to as the ESI.

Because the ET values used to compute the ESI are dependent on clear-sky conditions, only a portion of the ALEXI modeling domain can be filled on any given day.

On average, pixels in 75% of the CONUS domain are executed at least once every 6 days, and 95% are updated at least every 20 days. Therefore, temporal compositing of clear-sky f_{PET} values is required to fill in the full model domain. Compositing also serves to reduce effects of noise in the ET retrievals, primarily arising from incomplete cloud clearing in the LST inputs to ALEXI. ESI composites can be generated for multiple intervals to reflect different timescales of drought, analogous to the production of the Standardized Precipitation Indices. Here we examine composites computed over a moving window of 1, 2, and 3 months and a 6 month window defining the nominal growing season average for April through September. Composites are computed as an unweighted average of all index values that passed cloud-screening tests over the interval in question:

$$\langle v(w, y, i, j) \rangle = \frac{1}{nc} \sum_{n=1}^{nc} v(n, y, i, j) \quad (7.5)$$

where $\langle v(w, y, i, j) \rangle$ is the composite for week w , year y , and i, j grid location; $v(n, y, i, j)$ is the value on day n ; and nc is the number of clear days during the compositing interval.

To highlight differences in moisture conditions between years, drought indices are typically presented as anomalies or percentiles with respect to multiyear average fields determined over some period of record. Standardized anomalies in f_{PET} were computed over the period 2000–2009 and are expressed as a pseudo z-score, normalized to a mean of 0 and a standard deviation of 1. Fields describing “normal” (mean) conditions and temporal standard deviations at each pixel were computed for each compositing interval. Then standardized anomalies were computed as

$$\Delta \langle v(w, y, i, j) \rangle = \frac{\langle v(w, y, i, j) \rangle - \frac{1}{ny} \sum_{y=1}^{ny} \langle v(w, y, i, j) \rangle}{\sigma(w, i, j)} \quad (7.6)$$

where the second term in the numerator defines the normal field, averaged over all years ny , and the denominator is the standard deviation, also computed over all years.

In this notation, ESI-X is defined as $\Delta \langle f_{PET} \rangle$ computed for an X-month f_{PET} composite. Like most other drought indices, this formulation generates negative values when conditions are drier than normal and positive values for wetter than normal conditions. Implicit in the application of Equation 7.6 to ALEXI f_{PET} is the assumption that these quantities are normally distributed in time at every i, j location in the CONUS grid during 2000–2009. In this case, values of ESI less than -2 represent dry conditions exceeding 2σ , which should occur 2% of the time. At present, there are not enough years in the ALEXI archive (10 points) to warrant fitting of a non-normal distribution, but such adjustments may be applied as the archive’s length of record is extended.

7.4 PRECIPITATION-BASED DROUGHT METRICS

To better understand the behavior the new ET index, Anderson et al. (2011a) conducted an intercomparison with more commonly used drought indices based on precipitation observations. The suite of precipitation indices considered in the intercomparison is listed in Table 7.1 and described briefly in the following.

7.4.1 PALMER INDICES

The Palmer indices examined here include the Palmer Drought Severity Index (PDSI; Palmer, 1965), the Palmer Modified Drought Severity Index (PMDI; Heddingshaus and Sabol, 1991), the short-term (monthly timescale) Palmer Z Index, and the longer-term Palmer Hydrological Drought Index (PHDI). The principle advantages of the Palmer indices are a long period of record and a long history of usage, which has fostered familiarity within the drought community. However, the Palmer indices do have some specific limitations, which are reviewed in detail by Alley (1984) and Karl (1983). These limitations relate to lack of spatial and temporal standardization, along with simplistic treatment of evaporative losses and soil moisture storage.

Palmer-Z, PDSI, PMDI, and PHDI data sets are distributed by the National Climatic Data Center (NCDC) at the climate division level and on a monthly time step from 1895 to present (<http://www1.ncdc.noaa.gov/pub/data/cirs/>). These products are based on rain gauge and air temperature data that have been spatially averaged at the climate division scale (Guttman and Quayle, 1996). For this study, these Palmer data sets were regridded to the 10 km ALEXI grid for the study period, maintaining a constant index value over each of the climate division polygons.

7.4.2 STANDARDIZED PRECIPITATION INDEX

Issues with PDSI and variants thereof inspired the formation of the SPI (McKee et al., 1993, 1995), which uses observed precipitation as its only input. Precipitation data at a given location are converted into probabilities based on a local long-term climatology.

TABLE 7.1
Drought Indicators Included in the Intercomparison Study

Index	Acronym	Type
U.S. Drought Monitor	USDM	Multi-index synthesis
Evaporative Stress Index (X-month composite)	ESI-X	Remote sensing of f_{PET}
Standardized Precipitation Index (X-month)	SPI-X	Precipitation
Palmer Z Index	Z	Precipitation + storage
Palmer Drought Severity Index	PDSI	Precipitation + storage
Palmer Modified Drought Index	PMDI	Precipitation + storage
Palmer Hydrological Drought Index	PHDI	Precipitation + storage

The probabilities are then standardized such that a value of 0 indicates the median precipitation amount (in comparison with the climatology), which is measured at that pixel over the time interval in question (Edwards and McKee, 1997). The SPI can be computed for multiple timescales (typically ranging from 2 to 52 weeks) to monitor both short- and long-term drought conditions. Because the SPI is based only on precipitation data, a long period of record spanning many decades can be constructed. A major disadvantage of the SPI (and the Palmer indices) for mapping applications is that high-quality gridded precipitation data are not available at high spatial resolution for most parts of the world. In addition, lack of a temperature component means there is no accounting for rate of atmospheric consumption through evaporation.

SPI data are distributed by NCDC at the climate division level and on a monthly time step from 1895 to present (<http://www1.ncdc.noaa.gov/pub/data/cirs/>). These products are based on gauge data spatially averaged to the climate division scale. In this analysis, we have evaluated 1, 2, 3, and 6 month SPI products (referred to as SPI-1, SPI-2, SPI-3, and SPI-6, respectively). Longer SPI products (e.g., 9 and 12 months) extend beyond the annual growing season extent of the current ESI archive and will be assessed in a future study when the archive has been expanded to year round. The SPI data sets were regridded to the 10km ALEXI grid, maintaining a constant index value over each of the climate division polygons.

7.4.3 U.S. DROUGHT MONITOR

Through expert analysis, authors of the weekly USDM subjectively integrate information from many drought indicators, including the Palmer indices and the SPI, other hydrological parameters such as streamflow and groundwater, and local reports from state climatologists and observers across the country (Svoboda et al., 2002). Archived USDM data are distributed by the National Drought Mitigation Center (NDMC) at <http://drought.unl.edu/dm/> in both tabular and vector GIS formats. USDM data were downloaded in table form; these data report the percent area of each USDM drought class by calendar date at the county level.

County polygons were used to assign a USDM value for each date to each pixel in the 10km ALEXI grid. All pixels contained within a given county polygon were assigned the same value, corresponding to the most severe drought class observed over at least 33% of the county. For computational purposes, the drought classes were mapped to numerical values, with “no drought” assigned a value of -1 , $D0 = 0$ (abnormally dry), $D1 = 1$ (moderate drought), $D2 = 2$ (severe drought), $D3 = 3$ (extreme drought), and $D4 = 4$ (exceptional drought). For example, if a particular county was classified as 38% $D1$, and 0% $D2-4$, the pixels in that county were assigned a value of 1.

The USDM is unique among the drought indicators examined here in that it includes information at multiple drought timescales, as well as some socioeconomic and management/policy considerations. Because it is a subjective assessment, it should not be considered an absolute metric of “truth” in drought monitoring. Still, it is useful to assess spatiotemporal correlations between the USDM and various indicators used in its construction. This process gives us insight as to how new indices like the ESI can be most effectively used to inform production of the USDM.

7.4.4 STANDARDIZED ANOMALIES AND SEASONAL COMPOSITES

The Palmer and SPI data used here were normalized by the NCDC to the period 1931–1990. The period of record for the ESI (2000–2009) is considerably shorter, with average climatic conditions that are not necessarily representative of the normalization periods for the other indices. Therefore, the terms *wetter* and *drier* may convey different meaning for the ESI than for the PDSI and SPI. To improve comparability between the indices evaluated here, anomalies for each precipitation-based index included in the intercomparison, and for the USDM drought classes, were recomputed over the period 2000–2009 using Equation 7.6, analogous to the ESI formulation. Recomputation of anomalies with respect to the same period of record significantly improved spatial agreement between indices.

7.5 DROUGHT INDEX INTERCOMPARISON

7.5.1 SEASONAL ANOMALIES

Annual standardized anomalies in several drought indicators are compared in Figure 7.2, computed from 6 month composites (April–September) over the 2000–2009 growing seasons. The metrics displayed include anomalies in USDM drought classifications, the ESI, and three standard precipitation-based drought indices (Palmer-Z, SPI-3, and PDSI), which were selected to exemplify a range in timescales and modeling approaches. A visual intercomparison is useful in determining what new utility a satellite-based index like ESI can contribute to the effort of drought monitoring in the United States by placing its performance within the context of more familiar drought metrics. It also highlights the difficulty in forming a single objective synthesis of information conveyed by a diversity of drought indices.

In examining Figure 7.2, a few caveats should be considered. First, the USDM is not necessarily independent of the Palmer and SPI indices, as these are commonly used in the delineation of USDM drought classifications. In contrast, the ESI constitutes a completely independent assessment of surface moisture status because it does not use precipitation data as input and it is not currently used in the construction of the USDM. Second, USDM drought classes incorporate information relevant to different kinds of drought over varying timescales, and we cannot expect a single indicator to agree perfectly with the USDM. For example, some drought features in the USDM may indicate increased human demand for water (e.g., due to urban expansion) rather than natural hydrologic deficits, yet such impacts will not be conveyed in the ESI, SPI, or Palmer indices. Socioeconomic droughts cannot be easily identified solely by using remote sensing or meteorological data.

In Figure 7.2, drought features apparent in the USDM anomalies are generally reflected in one or more of the other indices, depending on the type and timescale of the drought event. An exception is the multiyear hydrological drought in the western United States in 2004, which is not well delineated by any of the indices included in the intercomparison. Such events should become evident in longer-term ESI composites (e.g., 12–24 months) once a year-round archive has been developed. In other years, the ESI successfully reproduces patterns evident in the precipitation indices, indicating the value of the LST signal as a surface moisture proxy. For example,

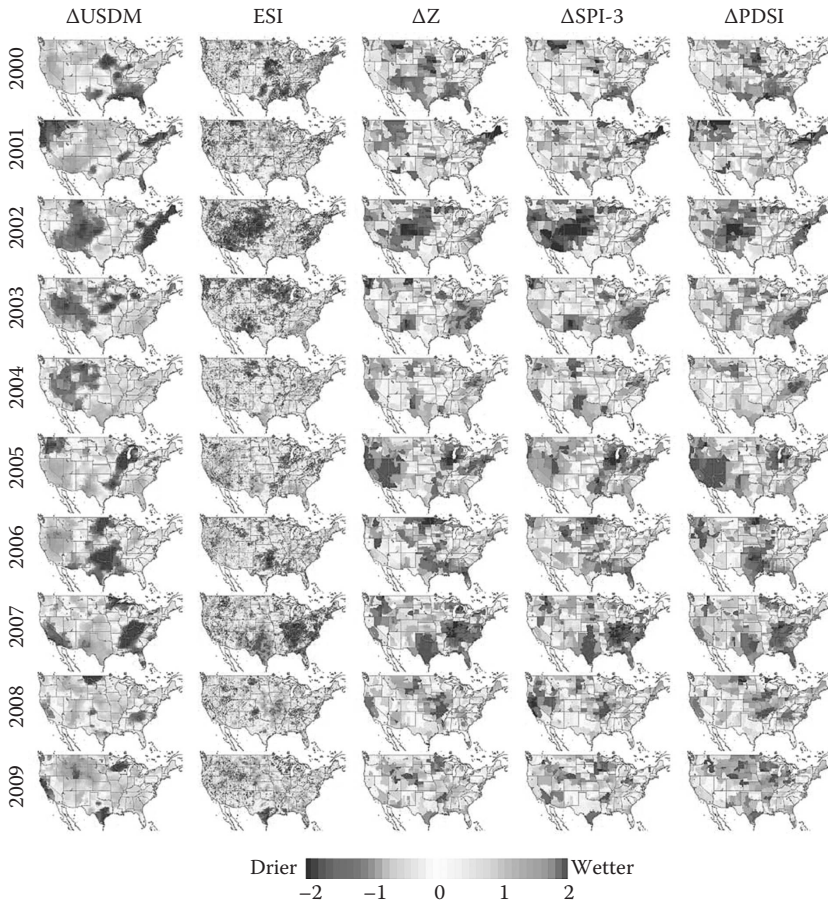


FIGURE 7.2 (See color insert.) Seasonal (26 week) anomalies in USDM, ESI, Z, SPI-3, and PDSI for 2000–2009. All indices are presented as z-scores or standard deviations from mean values determined over the 2000–2009 period.

the thermal band inputs to ALEXI capture the major drought events occurring in 2002 and 2007, even in the eastern United States, where there is dense vegetation cover during the middle of the growing season and little direct exposure of the dry soil surface.

Figure 7.3 looks in greater detail at the drought of 2007 that ravaged much of the southeastern United States (particularly in Alabama, Georgia, and the Carolinas), leading to low streamflows, depleted water supplies, and significant agricultural losses. This is a part of the CONUS where standard soil moisture retrievals based on passive microwave (MW) remote sensing tend to lose sensitivity because of strong attenuation of the soil signal by water contained in the dense forest canopy, as demonstrated in Figure 7.3c. In the thermal-derived ESI, however, the moisture deficit signal is strong—vegetation stress and soil moisture depletion in the surface skin contribute to elevated canopy and soil components of the composite surface radiometric

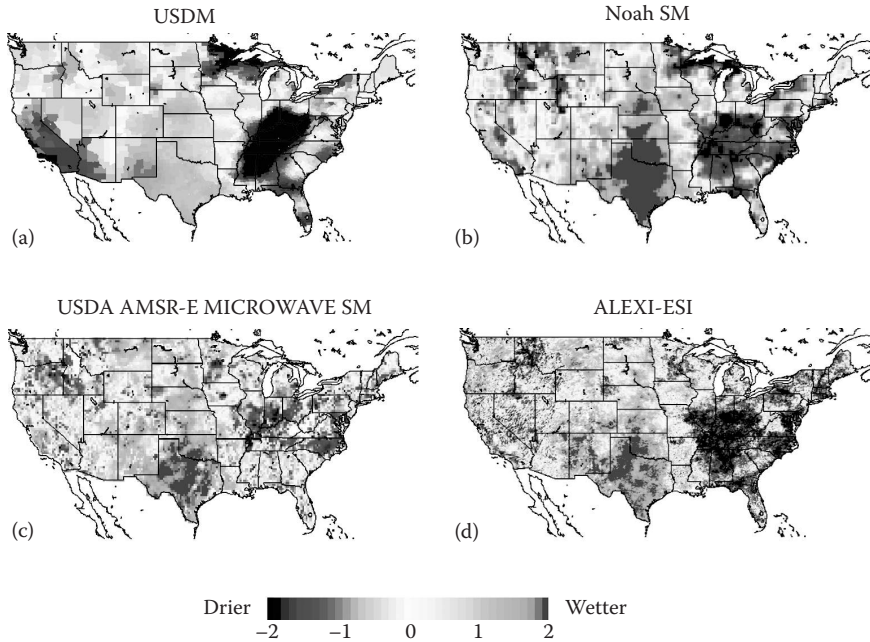


FIGURE 7.3 (See color insert.) Standardized anomalies for the 2007 growing season (April–September) in (a) the USDM drought classes, (b) soil moisture predicted by the Noah LSM, (c) USDA AMSR-E passive MW soil moisture retrieval, and (d) ALEXI-ESI.

temperature. The ESI reproduces patterns in soil moisture predicted by the Noah LSM (part of the Land Data Assimilation System [LDAS] modeling suite; Mitchell et al., 2004), with the advantage of requiring no antecedent precipitation information or soil texture data.

7.5.2 MONTHLY COMPARISONS

Using shorter timescale ESI composites, we can examine how quickly the ESI responds to changing moisture conditions. Figure 7.4 looks at delineations of drought conditions at monthly time steps in 1 and 3 month ESI composites over the southeastern United States during the drought of 2007, in comparison with anomalies in the Palmer Z index and the USDM. Temporal variability in the ESI-1 shows good general correspondence with monthly rainfall amounts evident in the Z index. For example, heavy rains in July led to short-term increases in ET, followed by re-intensified evaporative stress in August in response to anomalously low rainfall that month. Spatial patterns in monthly rainfall expressed in the Z-index maps are also reproduced with reasonable fidelity in the monthly ESI-1 maps.

In contrast, the longer-term ESI-3 better follows the monthly evolution in the USDM drought classifications, which are relatively conservative and typically do not change at the county level by more than one drought class between weekly reports. Anderson et al. (2011a) found that temporal correlations between the ESI and anomalies in the longer-term drought indicators included in the intercomparison

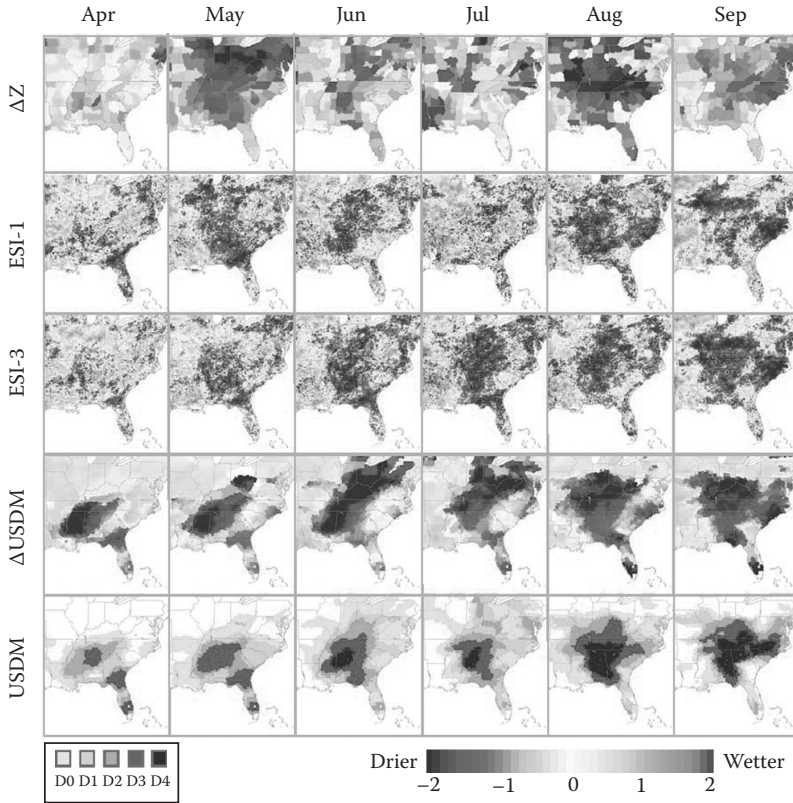


FIGURE 7.4 (See color insert.) Maps of monthly drought indicators during April–September 2007, focusing on the severe drought event that occurred in the southeastern United States.

(USDM PMDI, PHDI, PDSI, and SPI-6) improve with increasing ESI compositing interval, reaching a plateau at approximately 2–3 months. Again, good spatial correspondence is observed between patterns in monthly ESI-3 and Δ USDM, including formation of a hot spot over the Carolinas and Virginia in September, along with a pocket of reduced stress over southeast Georgia.

7.5.3 SPATIOTEMPORAL CORRELATIONS BETWEEN INDICES

Anderson et al. (2011a) examined spatial and temporal correlations between monthly ESI and several drought indicators, including the USDM, and these analyses are extended here. Table 7.2 lists spatial correlation coefficients computed between pairs of monthly drought index maps, averaged over the growing season months (April to September) for all years included in the intercomparison (2000–2009). These statistics help show which indicators most closely resemble other indicators in terms of monthly spatial patterns. All indicators were aggregated to the climate division scale prior to correlation computation. Temporal correlation coefficients between monthly indicators, computed at each pixel and averaged over the modeling domain, yield

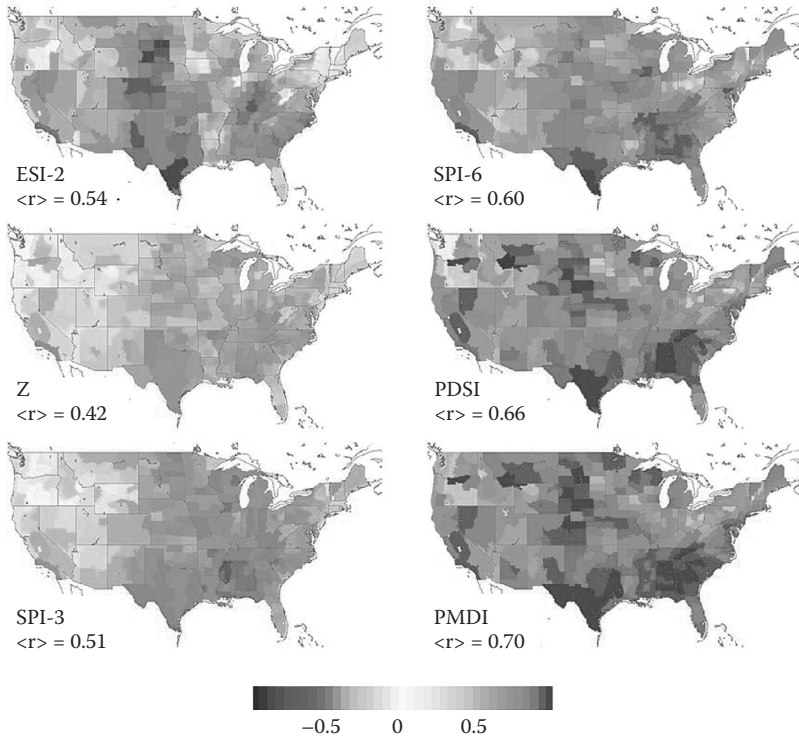


FIGURE 7.5 (See color insert.) Coefficient of temporal correlation between monthly maps of USDM anomalies and other drought indices included in the intercomparison for 2000–2009. Domain-averaged values of correlation coefficient are indicated as $\langle r \rangle$. To compute correlations, the ESI has been aggregated up to the climate division scale—the native resolution of the precipitation-based indices.

similar results (Anderson et al., 2011a). Maps of temporal correlation between the USDM and several drought indices are shown in Figure 7.5.

In terms of monthly spatial patterns over the growing season, the USDM is most strongly correlated with the PMDI ($\langle r \rangle = 0.71$; Table 7.2). Spatial agreement with the USDM improves as index timescale increases (e.g., from SPI-1 to SPI-6). The modifications to the PDSI embedded within the PMDI formulation result in improved agreement with USDM anomalies (and with most other indices), suggesting that these modifications have had a positive impact by improving spatial comparability across the CONUS domain. It must be remembered, however, that the precipitation indices in Table 7.2 (Palmer and SPI) are used in the construction of the USDM and, therefore, are not independent estimators of drought conditions. This will lead to enhanced correlations with USDM drought classes.

In contrast, the ESI can be considered a truly independent indicator within the context of this intercomparison. Both ESI-2 and -3 maps yield similar spatial correlation ($\langle r \rangle = 0.52$) with the USDM, ranking between those of SPI-3 and SPI-6 (0.51 and 0.60, respectively). This suggests that ET, as a physical process, integrates over a

longer time period than the equivalent precipitation interval—that is, it retains some memory of moisture conditions prior to the composite interval. In terms of pixel-based temporal correlation, Anderson et al. (2011a) demonstrated that the shorter-term precipitation indices (Z and SPI-1 to SPI-3) show a weakly negative correlation with USDM rankings in the northwestern United States (see [Figure 7.5](#)), which may be related to hydrologic delays in snowpack-forming regions (Shukla and Wood, 2008). In addition, the 1, 2, and 3 month SPIs show weaker correlations with the USDM in the southwestern United States. Wu et al. (2007) argue that distributions of the 3 month SPI are highly skewed in arid climates, peaking strongly in the no-rain case and causing SPI-3 to underpredict the severity and frequency of drought events. The 6 month SPI has a more normal distribution and better represents the observed drought occurrence frequency. This is consistent with the results of Anderson et al. (2011a) shown in [Figure 7.5](#), which indicate that SPI-6 is more highly correlated with the USDM in the western United States than SPI-3.

The ESI does not exhibit the strongly degraded performance in the western United States seen in SPI products of comparable timescale ([Figure 7.5](#)). Drought rankings by the ESI and the USDM are most highly correlated in time over the Great Plains and in the southern United States. These are areas where LST and indicators of vegetation fraction, like the Normalized Difference Vegetation Index (NDVI), tend to be anticorrelated through much of the April–September period (see [Figure 7.4](#) in Karnieli et al., 2010), indicating moisture-limiting (as opposed to energy-limiting) vegetation growth conditions. ET will be most sensitive to changing subsurface moisture conditions under these conditions. Of the indices considered here, the ESI is most similar to the PMDI, with agreement improving with ESI compositing interval ([Table 7.2](#)). We anticipate that ESI agreement with USDM and PMDI will further improve when snow processes have been incorporated into ALEXI and longer timescale ESI moving composite intervals (e.g., 6 and 12 months) become more robust (see [Section 7.6](#)).

7.6 LIMITATIONS AND FUTURE WORK

Operational execution of the ALEXI model is being transitioned to the National Environmental Satellite, Data, and Information Service (NESDIS) within NOAA in support of the monthly North American Drought Briefing generated by the Climate Prediction Center (<http://www.cpc.noaa.gov/products/Drought/>). As part of this transition, model preprocessing infrastructure is being reconfigured to use standard NOAA data sources. Hourly skin temperature and insolation will be obtained from the NESDIS GOES Surface and Insolation Product (GSIP; www.star.nesdis.noaa.gov/smcd/opdb/goes/gcip/html/gsip_home.html). Downwelling long-wave radiation at the earth's surface (needed to compute net radiation) is also provided within the GSIP product suite. Ultimately, the ESI archive can be extended back to 1979 using GOES imagery archived at the NCDC through the International Satellite Cloud Climatology Project (ISCCP) B1 Data Rescue project. Meteorological inputs to ALEXI (primarily wind speed and lapse rate) will be extracted from the Regional Climate Data Assimilation System (R-CDAS)—the real-time continuation of the North American Regional Reanalysis (NARR) performed by the National Centers

for Environmental Prediction (NCEP) Environmental Modeling Center (EMC) (Mesinger et al., 2006). While ESI evaluation is currently limited to snow-free periods coincident with the growing season for most of the CONUS (approximately April–October), a snow energy balance modeling component in TSEB, adapted from the work of Kongoli and Bland (2000), is under development to provide year-round coverage. Improved treatment of winter ET processes will allow assessment of longer-term ESI composites (e.g., 6–12 months), which may better characterize impacts of hydrological droughts.

The spatial domain of ALEXI-ESI application is also undergoing expansion. As part of the transition to NESDIS, the domain will expand to include North and South America (approximately -60° to $+60^\circ$ latitude) using GOES data. Other domains are being established over southern Europe, the Middle East, and the African continent using land-surface products from the European Meteosat Second Generation (MSG) satellites (Anderson et al., 2011b). A longer-term goal of global ESI coverage (excluding the poles) can be obtained with the current international system of geostationary satellites, as archived at hourly time steps and 5 km resolution by the Geoland2 project under the European GMES (Global Monitoring for Environment and Security) initiative (Lacaze et al., 2010), or using the ISCCP B1 data set at 3 hourly temporal and 10 km spatial resolution (Knapp, 2008).

Work is underway to improve the spatial resolution of ESI products over targeted regions (e.g., the U.S. Corn Belt), employing a multisensor fusion strategy to map daily ET and f_{PET} at 30 m resolution. Using DisALEXI, daily ALEXI fields at 10 km can be downscaled to 1 km using TIR data from MODIS (available every 1–2 days) and to 30 m using Landsat TIR imagery (60–120 m native resolution and 8–16 day revisit depending on the number of satellites concurrently in orbit) that has been improved to the spatial resolution of the shortwave bands (30 m) using a thermal sharpening technique (Agam et al., 2008; Kustas et al., 2003). Finally, a new Spatial and Temporal Adaptive Reflectance Model (STARFM; Gao et al., 2006) can be used to merge the MODIS and Landsat-scale ET evaluations, generating daily predicted fields at the Landsat scale (Anderson et al., 2011b). In this way, we make full use of all available TIR data in interpolating surface moisture conditions between infrequent Landsat overpasses. The 30 m resolution will enable sub-field-scale sampling, leading to more robust assessments of vegetation condition in agricultural landscapes and other ecosystems with small-scale heterogeneity (Figure 7.6).

One of the major limitations of TIR-based indices is the inability to collect thermal images of the land surface through cloud cover. This can severely limit update capacity in perpetually cloudy regions of the globe, such as in the Intertropical Convergence Zone. Temporal sampling can be improved by incorporating moisture information during cloudy periods retrieved using MW remote sensing—for example, using the Advanced Microwave Scanning Radiometer-Earth Observing System (AMSR-E) and instruments on the upcoming Soil Moisture Active Passive (SMAP) mission. Hain (2010) showed that joint assimilation of TIR f_{PET} (from ALEXI) and MW soil moisture into the Noah LSM in NLDAS provides better soil moisture estimates than either retrieval method (TIR or MW) does in isolation. The two retrievals are quite complementary: TIR provides relatively high resolution (60 m–10 km) and low temporal resolution (due to cloud cover) retrievals over a wide

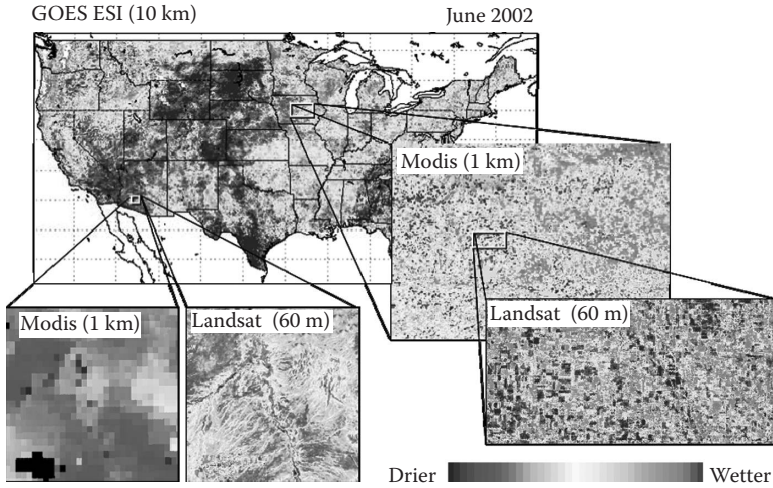


FIGURE 7.6 (See color insert.) Comparison of spatial information content provided by ESI fields generated from GOES, MODIS, and Landsat TIR imagery. In this figure, red indicates drier conditions and green indicates wetter conditions.

range of vegetation cover fraction, while MW provides relatively low spatial resolution (10–50 km) and high temporal resolution (can penetrate through clouds), but accurate retrievals are only possible over areas with sparse vegetation. Furthermore, MW retrievals are sensitive to soil moisture only in the shallow soil surface layer (0–5 cm), while TIR provides information about soil moisture conditions integrated over the full root zone, reflected in the observed canopy temperature. The added value of TIR assimilation over MW alone is most significant in areas of moderate to dense vegetation cover (greater than 60%, characterizing much of the eastern United States), where MW retrievals have little sensitivity to soil moisture at any depth due to absorption/emission by water contained within the vegetative canopy. Joint assimilation of both TIR f_{PET} and MW soil moisture into a prognostic LSM would serve to maximize both spatial and temporal sampling of surface moisture conditions, and provide additional hydrologic information such as runoff, streamflow, and groundwater recharge.

7.7 CONCLUSIONS

An intercomparison was conducted between drought indices based on remotely sensed ET, ground observations of rainfall, and drought classifications reported in the USDM during 2000–2009. The ESI, which represents anomalies in the ratio of actual to PET (f_{PET}) derived from thermal remote sensing, was demonstrated to provide useful information for routine monitoring of drought conditions at continental scales without requiring any knowledge of antecedent precipitation. Spatial distributions in ESI correlate with patterns in traditional precipitation-based drought indices, responding to rainfall events at monthly time steps. Therefore, this new drought index appears to be a valuable complement to standard precipitation indices.

ET and f_{PET} products from the LSM suite in NLDAS are also available over the CONUS and are employed as constituents of the NCEP North American Drought Briefing. The main benefit of the ALEXI approach is that it requires no prior information regarding antecedent precipitation and nonprecipitation moisture inputs or about soil moisture storage capacity—the current surface moisture status is deduced directly from the remotely sensed radiometric temperature signal. Thus, thermal remote-sensing models provide independent moisture information that can be useful for validating or updating spatially distributed soil moisture variables in prognostic land-surface water balance models and forecasts.

Because precipitation is not used in the construction of the ESI, this index will have utility for real-time monitoring in regions with sparse rainfall data or significant delays in meteorological reporting. Remote sensing provides a more complete sampling of land-surface conditions than do point-based surface measurement networks and, therefore, better facilitates upscaling to larger scales (Anderson et al., 2007a). High-resolution remote-sensing precipitation products exist (e.g., Joyce et al., 2004), but validation studies show that although these are reasonably good at predicting the occurrence of precipitation, they are less accurate at estimating precipitation amount (Zeweldi and Gebremichael, 2009), which is critical for assessing drought impact. Using multisensor data fusion, integrating TIR-based ET data from geostationary and polar orbiting systems, the ESI can potentially be generated at sub-field-scale resolutions.

The thermal remote-sensing inputs to the ESI can also identify signatures of moisture inputs that are not collocated with precipitation events (e.g., irrigation and wicking from shallow water tables), which may mitigate the impact of local rainfall deficits. Significant horizontal redistribution of precipitation will also be reflected in ESI. These additional moisture sources will not be represented in LSMs without prior knowledge of their existence. The ESI therefore conveys information about *actual* stress rather than the potential for stress. It reflects a different component of the hydrologic cycle that has typically not been considered in drought monitoring, focusing on water use rather than water supply. Inclusion of an ET-based index into the existing drought index suite may provide valuable information about “rapid-onset” events, a situation where intense hot, dry, and windy conditions lead to rapid water loss and the potential for catastrophic crop yield loss, especially when crops are newly emerged and immature. Such events have caused great economic damage in the United States and other parts of the world but are difficult to detect and explain using standard meteorological drought indices.

Future analyses will include comparisons with drought indices based on soil moisture and surface runoff estimates from the NLDAS LSM system, which are currently used in the North American Drought Briefing generated by the NOAA Climate Prediction Center (<http://www.cpc.noaa.gov/products/Drought/>), and with other remote-sensing drought indices, such as the Vegetation Health Index (VHI; Kogan, 1997) and the Vegetation Drought Response Index (VegDRI; Brown et al., 2008), and indicators from the Simplified Surface Energy Balance (SSEB) and Vegetation ET (VegET) approaches described by Senay et al. (2012; Chapter 6). The domain of ALEXI application is under expansion to provide global coverage between -60° and 60° latitude using the international system of

geostationary satellites. Finally, work is under way to incorporate a snow module in ALEXI so that it can be applied year-round as the archive is expanded retrospectively to the beginning of the GOES era (into the late 1970s) and forward in real time.

ACKNOWLEDGMENTS

Support for this work was provided by funding from the NOAA Climate Program Office under grant GC09-236. USDA is an equal opportunity provider and employer.

REFERENCES

- Agam, N., W.P. Kustas, M.C. Anderson, F. Li, and P.D. Colaizzi. 2008. Utility of thermal image sharpening for monitoring field-scale evapotranspiration over rainfed and irrigated agricultural regions. *Geophysical Research Letters* 35, doi:10.1029/2007GL032195.
- Alley, W.M. 1984. The Palmer Drought Severity Index: Limitations and assumptions. *Journal of Climate and Applied Meteorology* 23:1100–1109.
- Anderson, M.C., C.R. Hain, B. Wardlow, J.R. Mecikalski, and W.P. Kustas. 2011a. Evaluation of a drought index based on thermal remote sensing of evapotranspiration over the continental U.S. *Journal of Climate* 24:2025–2044.
- Anderson, M.C., W.P. Kustas, and J.M. Norman. 2007a. Upscaling flux observations from local to continental scales using thermal remote sensing. *Agronomy Journal* 99:240–254.
- Anderson, M.C., W.P. Kustas, J.M. Norman, C.R. Hain, J.R. Mecikalski, L. Schultz, M.P. Gonzalez-Dugo, C. Cammalleri, G. d’Urso, A. Pimstein, and F. Gao. 2011b. Mapping daily evapotranspiration at field to continental scales using geostationary and polar orbiting satellite imagery. *Hydrology and Earth System Sciences* 15:223–239.
- Anderson, M.C., J.M. Norman, G.R. Diak, W.P. Kustas, and J.R. Mecikalski. 1997. A two-source time-integrated model for estimating surface fluxes using thermal infrared remote sensing. *Remote Sensing of Environment* 60:195–216.
- Anderson, M.C., J.M. Norman, J.R. Mecikalski, J.P. Otkin, and W.P. Kustas. 2007b. A climatological study of evapotranspiration and moisture stress across the continental U.S. based on thermal remote sensing: II. Surface moisture climatology. *Journal of Geophysical Research* 112:D11112, doi:10.1029/2006JD007507.
- Anderson, M.C., J.M. Norman, J.R. Mecikalski, J.P. Otkin, and W.P. Kustas. 2007c. A climatological study of evapotranspiration and moisture stress across the continental U.S. based on thermal remote sensing: I. Model formulation. *Journal of Geophysical Research* 112: D10117, doi:10.1029/2006JD007506.
- Anderson, M.C., J.M. Norman, W.P. Kustas, F. Li, J.H. Prueger, and J.M. Mecikalski. 2005. Effects of vegetation clumping on two-source model estimates of surface energy fluxes from an agricultural landscape during SMACEX. *Journal of Hydrometeorology* 6:892–909.
- Brown, J.F., B.D. Wardlow, T. Tadesse, M.J. Hayes, and B.C. Reed. 2008. The Vegetation Drought Response Index (VegDRI): A new integrated approach for monitoring drought stress in vegetation. *GIScience and Remote Sensing* 45:16–46.
- Courault, D., B. Seguin, and A. Olioso. 2005. Review on estimation of evapotranspiration from remote sensing data: From empirical to numerical modeling approaches. *Irrigation and Drainage Systems* 19:223–239.
- Edwards, D.C. and T.B. McKee. 1997. Characteristics of 20th century drought in the United States at multiple time scales. Climatology Report Number 97-2, Colorado State University, Fort Collins, CO.

- Gao, F., J. Masek, M. Schwaller, and F.G. Hall. 2006. On the blending of the Landsat and MODIS surface reflectance: Predicting daily Landsat surface reflectance. *IEEE Transactions on Geoscience and Remote Sensing* 44:2207–2218.
- Guttman, N.B. and R.G. Quayle. 1996. A historical perspective of U.S. climate divisions. *Bulletin of the American Meteorological Society* 77:293–303.
- Hain, C.R. 2010. Developing a dual assimilation approach for thermal infrared and passive microwave soil moisture retrievals. PhD thesis, University of Alabama, Huntsville, AL.
- Heddinghaus, T.R. and P. Sabol. 1991. A review of the Palmer Drought Severity Index and where do we go from here? *Proceedings of the 7th Conference on Applied Climatology*, American Meteorological Society, Boston, MA.
- Huffman, G.J., R.F. Adler, D.T. Bolving, G. Gu, E.J. Nelkin, Y. Hong, D.B. Wolff, K.P. Bowman, and E.F. Stocker. 2007. The TRMM Multisatellite Precipitation Analysis (TMPA): Quasi-global, multiyear, combined-sensor precipitation estimates at fine scales. *Journal of Hydrometeorology* 8:38–55.
- Joyce, R.J., J.E. Janowiak, P.A. Arkin, and P. Xie. 2004. CMORPH: A method that produces global precipitation estimates from passive microwave and infrared data at high spatial and temporal resolution. *Journal of Hydrometeorology* 5:487–503.
- Kalma, J.D., T.R. McVicar, and M.F. McCabe. 2008. Estimating land surface evaporation: A review of methods using remotely sensing surface temperature data. *Surveys in Geophysics* 29(4–5):421–469.
- Karl, T.R. 1983. Some spatial characteristics of drought duration in the United States. *Journal of Climate and Applied Meteorology* 22:1356–1366.
- Karnieli, A., N. Agam, R.T. Pinker, M.C. Anderson, M.L. Imhoff, G.G. Gutman, N. Panov, and A. Goldberg. 2010. Use of NDVI and land surface temperature for drought assessment: Merits and limitations. *Journal of Climate* 23:618–633.
- Knapp, K.R. 2008. Scientific data stewardship of International Satellite Cloud Climatology Project B1 geostationary observations. *Journal of Applied Remote Sensing* 2:023548.
- Kogan, F.N. 1997. Global drought watch from space. *Bulletin of the American Meteorological Society* 78:621–636.
- Kongoli, C.E. and W.L. Bland. 2000. Long-term snow depth simulations using a modified atmosphere-land exchange model. *Agricultural and Forest Meteorology* 104:273–287.
- Kustas, W.P. and J.M. Norman. 1999. Evaluation of soil and vegetation heat flux predictions using a simple two-source model with radiometric temperatures for partial canopy cover. *Agricultural and Forest Meteorology* 94:13–29.
- Kustas, W.P. and J.M. Norman. 2000. A two-source energy balance approach using directional radiometric temperature observations for sparse canopy covered surfaces. *Agronomy Journal* 92:847–854.
- Kustas, W.P., G.R. Diak, and J.M. Norman. 2001. Time difference methods for monitoring regional scale heat fluxes with remote sensing. *Land Surface Hydrology, Meteorology, and Climate: Observations and Modeling* 3:15–29.
- Kustas, W.P., J.M. Norman, M.C. Anderson, and A.N. French. 2003. Estimating subpixel surface temperatures and energy fluxes from the vegetation index–radiometric temperature relationship. *Remote Sensing of Environment* 85:429–440.
- Labeledzki, L. and E. Kanecka-Geszke. 2009. Standardized evapotranspiration as an agricultural drought index. *Irrigation and Drainage* 58:607–616.
- Lacaze, R., G. Balsamo, F. Baret, A. Bradley, J.-C. Calvet, F. Camacho, R. D’Andrimont, S.C. Freitas, H. Makhlara, V. Naeimi, P. Pacholczyk, H. Poilvé, B. Smets, K. Tansey, I.F. Trigo, W. Wagner, and M. Weiss. 2010. Geoland2—Towards an operational GMES land monitoring core service; First results of the biogeophysical parameter core mapping service. In *ISPRS TC VII Symposium—100 Years ISPRS*, Vienna, Austria, July 5–7, 2010, eds. W. Wagner and B. Székely, IAPRS, Vol. XXXVIII, Part 7B, pp. 354–359.

- Li, H., Y. Lei, L. Zheng, and R. Mao. 2005. Calculating regional drought indices using evapotranspiration (ET) distribution derived from Landsat7 ETM+ data. In *Remote Sensing and Modeling of Ecosystems for Sustainability II* (Proceedings Volume 5884), eds. W. Gao and D.R. Shaw. Bellingham, Washington, DC: SPIE.
- McEnery, J., J. Ingram, Q. Duan, T. Adams, and L. Anderson. 2005. NOAA's Advanced Hydrologic Prediction Service. *Bulletin of the American Meteorological Society* 86:375–385.
- McKee, T.B., N.J. Doesken, and J. Kleist. 1993. The relationship of drought frequency and duration to time scales. *Preprints, 8th Conference on Applied Climatology*, Anaheim, CA.
- McKee, T.B., N.J. Doesken, and J. Kleist. 1995. Drought monitoring with multiple time scales. *Preprints, 9th Conference on Applied Climatology*, Dallas, TX.
- McNaughton, K.G. and T.W. Spriggs. 1986. A mixed-layer model for regional evaporation. *Boundary-Layer Meteorology* 74:262–288.
- Mecikalski, J.M., G.R. Diak, M.C. Anderson, and J.M. Norman. 1999. Estimating fluxes on continental scales using remotely-sensed data in an atmosphere-land exchange model. *Journal of Applied Meteorology* 38:1352–1369.
- Mesinger, F., G. DiMego, E. Kalnay, K. Mitchell, P.C. Shafran, W. Ebisuzaki, D. Jovic, J. Woollen, E. Rogers, E.H. Berbery, M.B. Ek, Y. Fan, R. Grumbine, W. Higgins, H. Li, Y. Lin, G. Manikin, D. Parrish, and W. Shi. 2006. North American regional reanalysis. *Bulletin of the American Meteorological Society* 87:343–360.
- Mitchell, K.E., D. Lohmann, P.R. Houser, E.F. Wood, J.C. Schaake, A. Robock, B.A. Cosgrove, J. Sheffield, Q. Duan, L. Luo, R.W. Higgins, R.T. Pinker, J.D. Tarpley, D.P. Lettenmaier, C.H. Marshall, J.K. Entin, M. Pan, W. Shi, V. Koren, J. Meng, B.H. Ramsay, and A.A. Bailey. 2004. The multi-institution North American Land Data Assimilation System (NLDAS): Utilizing multiple GCIP products and partners in a continental distributed hydrological modeling system. *Journal of Geophysical Research* 190:D07S90, doi:10.1029/2003JD003823.
- Mo, K.C., L.N. Long, Y. Xia, S.K. Yang, J.E. Schemm, and M.B. Ek. 2010. Drought indices based on the Climate Forecast System Reanalysis and ensemble NLDAS. *Journal of Hydrometeorology* 12:181–205. doi: 10.1175/2010JHM1310.1171.
- Moran, M.S. 2003. Thermal infrared measurement as an indicator of plant ecosystem health. In *Thermal Remote Sensing in Land Surface Processes*, eds. D.A. Quattrochi and J. Luvall, 257–282. Boca Raton, FL: CRC Press, Taylor & Francis Group.
- Norman, J.M., M.C. Anderson, W.P. Kustas, A.N. French, J.R. Mecikalski, R.D. Torn, G.R. Diak, T.J. Schmugge, and B.C.W. Tanner. 2003. Remote sensing of surface energy fluxes at 10¹-m pixel resolutions. *Water Resources Research* 39(8), doi:10.1029/2002WR001775.
- Norman, J.M., M. Divakarla, and N.S. Goel. 1995b. Algorithms for extracting information from remote thermal-IR observations of the earth's surface. *Remote Sensing of Environment* 51:157–168.
- Norman, J.M., W.P. Kustas, and K.S. Humes. 1995a. A two-source approach for estimating soil and vegetation energy fluxes from observations of directional radiometric surface temperature. *Agricultural and Forest Meteorology* 77:263–293.
- Palmer, W.C. 1965. Meteorological drought. Research Paper 45, U.S. Department of Commerce Weather Bureau, Washington, DC.
- Priestley, C.H.B. and R.J. Taylor. 1972. On the assessment of surface heat flux and evaporation using large-scale parameters. *Monthly Weather Review* 100:81–92.
- Schaake, J.C., Q. Duan, V. Koren, K.E. Mitchell, P.R. Houser, E.F. Wood, A. Robock, D.P. Lettenmaier, D. Lohmann, B. Cosgrove, J. Sheffield, L. Luo, R.W. Higgins, R.T. Pinker, and J.D. Tarpley. 2004. An intercomparison of soil moisture fields in the North American Land Data Assimilation System (NLDAS). *Journal of Geophysical Research* 109, doi:10.1029/2002JD00309.

- Senay, G.B., S. Bohms, and J.P. Verdin. 2012. Remote sensing of evapotranspiration for operational drought monitoring using principles of water and energy balance. In *Remote Sensing of Drought: Innovative Monitoring Approaches*, eds. B.D. Wardlow, M.C. Anderson, and J.P. Verdin. Boca Raton, FL: CRC Press.
- Shukla, S. and A.W. Wood. 2008. Use of a standardized runoff index for characterizing hydrologic drought. *Geophysical Research Letters* 35, doi:10.1029/2007GL032487.
- Svoboda, M., D. LeComte, M. Hayes, R. Heim, K. Gleason, J. Angel, B. Rippey, R. Tinker, M. Palecki, D. Stooksbury, D. Miskus, and S. Stephens. 2002. The U.S. Drought Monitor. *Bulletin of the American Meteorological Society* 83:1181–1190.
- Villarini, G., W.F. Krajewski, and J.A. Smith. 2009. New paradigm for statistical validation of satellite precipitation estimates: Application to a large sample of the TMPS 0.25° 3-hourly estimates over Oklahoma. *Journal of Geophysical Research* 114:D12106, doi:12110.11029/12008JD011475.
- Wu, H., M.D. Svoboda, M.J. Hayes, D.A. Wilhite, and F. Wen. 2007. Appropriate application of the Standardized Precipitation Index in arid locations and dry seasons. *International Journal of Climatology* 27:65–79.
- Zeweldi, D.A. and M. Gebremichael. 2009. Evaluation of CMORPH Precipitation Products at fine space-time scales. *Journal of Hydrometeorology* 10:300–307.

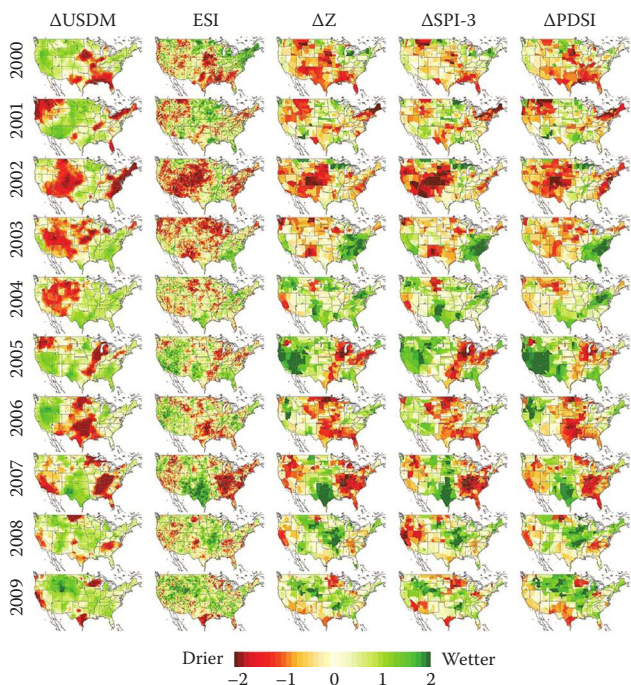


FIGURE 7.2 Seasonal (26 week) anomalies in USDM, ESI, Z, SPI-3, and PDSI for 2000–2009. All indices are presented as z-scores or standard deviations from mean values determined over the 2000–2009 period.

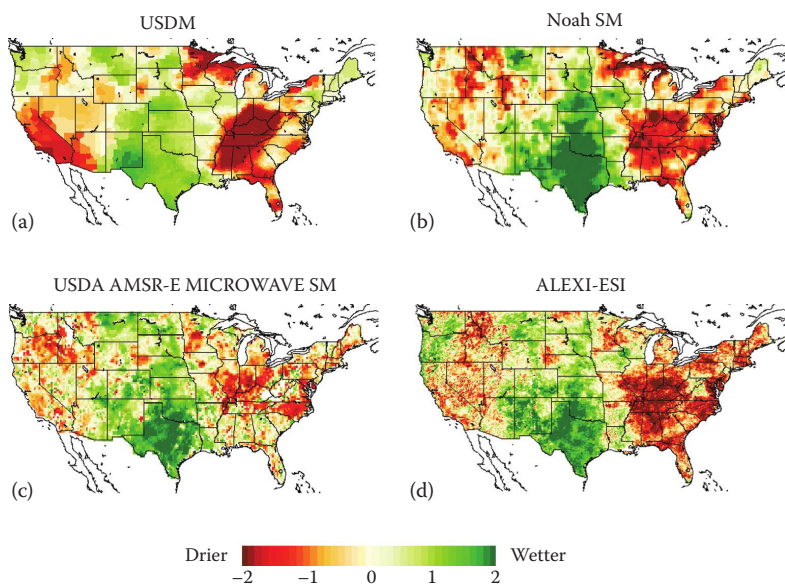


FIGURE 7.3 Standardized anomalies for the 2007 growing season (April–September) in (a) the USDM drought classes, (b) soil moisture predicted by the Noah LSM, (c) USDA AMSR-E passive MW soil moisture retrieval, and (d) ALEXI-ESI.

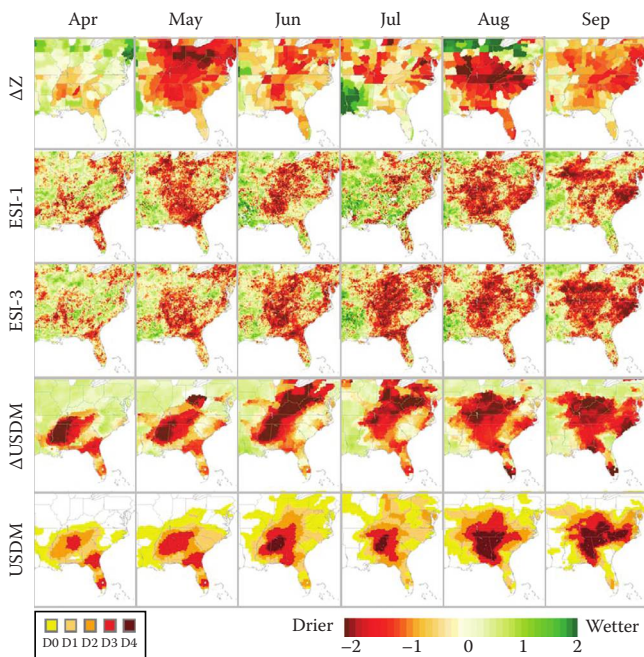


FIGURE 7.4 Maps of monthly drought indicators during April–September 2007, focusing on the severe drought event that occurred in the southeastern United States.

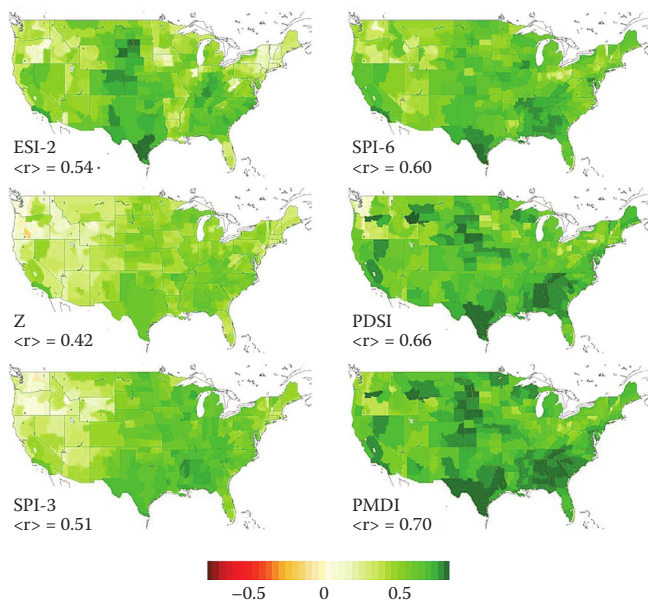


FIGURE 7.5 Coefficient of temporal correlation between monthly maps of USDM anomalies and other drought indices included in the intercomparison for 2000–2009. Domain-averaged values of correlation coefficient are indicated as $\langle r \rangle$. To compute correlations, the ESI has been aggregated up to the climate division scale—the native resolution of the precipitation-based indices.

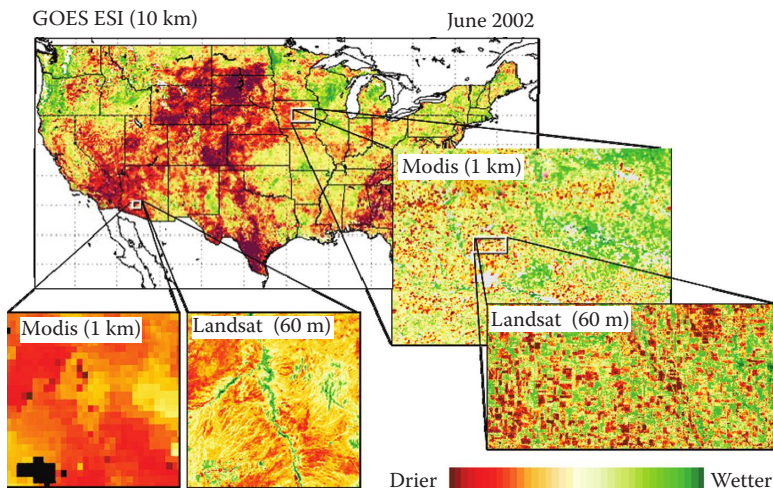


FIGURE 7.6 Comparison of spatial information content provided by ESI fields generated from GOES, MODIS, and Landsat TIR imagery. In this figure, red indicates drier conditions and green indicates wetter conditions.